

In situ monitoring redox processes in energy storage using UV–Vis spectroscopy

Zhang, Danzhen; Wang, Ruocun (John); Wang, Xuehang; Gogotsi, Yury

DOI

[10.1038/s41560-023-01240-9](https://doi.org/10.1038/s41560-023-01240-9)

Publication date

2023

Document Version

Final published version

Published in

Nature Energy

Citation (APA)

Zhang, D., Wang, R., Wang, X., & Gogotsi, Y. (2023). In situ monitoring redox processes in energy storage using UV–Vis spectroscopy. *Nature Energy*, 8(6), 567-576. <https://doi.org/10.1038/s41560-023-01240-9>

Important note

To cite this publication, please use the final published version (if applicable). Please check the document version above.

Copyright

Other than for strictly personal use, it is not permitted to download, forward or distribute the text or part of it, without the consent of the author(s) and/or copyright holder(s), unless the work is under an open content license such as Creative Commons.

Takedown policy

Please contact us and provide details if you believe this document breaches copyrights. We will remove access to the work immediately and investigate your claim.

Green Open Access added to TU Delft Institutional Repository

'You share, we take care!' - Taverne project

<https://www.openaccess.nl/en/you-share-we-take-care>

Otherwise as indicated in the copyright section: the publisher is the copyright holder of this work and the author uses the Dutch legislation to make this work public.

In situ monitoring redox processes in energy storage using UV–Vis spectroscopy

Received: 27 August 2022

Accepted: 7 March 2023

Published online: 06 April 2023

 Check for updates

Danzhen Zhang ^{1,3}, Ruocun (John) Wang ^{1,3}, Xuehang Wang ^{1,2} ✉
& Yury Gogotsi ¹ ✉

Understanding energy storage mechanisms in electrochemical energy storage devices lays the foundations for improving their energy and power density. Here we introduce in situ ultraviolet–visible (UV–Vis) spectroscopy method to distinguish battery-type, pseudocapacitive and electrical double-layer charge storage processes. On the basis of $\text{Ti}_3\text{C}_2\text{T}_x$ MXene in aqueous acidic and neutral electrolytes, and lithium titanium oxide in an organic electrolyte, we found a correlation between the evolution of UV–Vis spectra and the charge storage mechanism. The electron transfer number for $\text{Ti}_3\text{C}_2\text{T}_x$ in an acidic electrolyte was calculated using quantitative analysis, which was close to previous measurements using X-ray absorption spectroscopy. Further, we tested the methodology to distinguish the non-Faradaic process in $\text{Ti}_3\text{C}_2\text{T}_x$ MXene in a water-in-salt electrolyte, despite well-defined peaks in cyclic voltammograms. In situ UV–Vis spectroscopy is a fast and cost-effective technique that effectively supplements electrochemical characterization to track changes in oxidation state and materials chemistry and determine the charge storage mechanism.

To satisfy the diverse requirements of power and energy density, it is critical to develop electrochemical energy storage technologies that use various charge storage mechanisms^{1,2}. While recent advances blur the boundaries between those charge storage processes, they can be broadly classified into three major kinds: battery-type redox, pseudocapacitive and electrical double-layer (EDL) storage^{3–5}. Battery-type charge storage is typically either diffusion- or nucleation-controlled Faradaic process, which is accompanied by electron transfer and phase transformations⁶. Electrical double-layer capacitors (EDLCs) store energy by non-Faradaic electrosorption of ions onto the surface of electrode materials, which leads to rapid charging and high power⁷. Pseudocapacitive charge storage features surface-controlled charge storage with higher energy density than EDLCs and greater power density than batteries.

An important question associated with these three mechanisms is: ‘how can researchers effectively distinguish the charge storage mechanisms for a particular electrode–electrolyte system?’ One popular method is cyclic voltammetry (CV). EDLCs feature almost rectangular

CV curves. Well-defined redox peaks with peak separations are shown in battery materials. Pseudocapacitive materials exhibit voltammogram features where cathodic and anodic branches ‘mirror’ each other at slow rates (<20 mV separation of reduction and oxidation peaks) due to fast surface-controlled redox reactions or no peaks at all (for example, MnO_2) (refs. 8,9). However, there are exceptions. For example, $\text{Ti}_3\text{C}_2\text{T}_x$ in 19.8 m LiCl water-in-salt electrolyte has well-defined peaks in the CV curves, but the actual mechanism is non-Faradaic solvated cation insertion¹⁰. Many efforts recently focused on novel materials and systems using intermediate or mixed charge storage mechanisms, which also depend on the potential window¹¹. Thus, determining charge storage mechanisms by CV measurement is difficult in these systems.

Due to the variety and complexity of compositional/structural changes in electrode materials during charge storage, advanced in situ or ex situ characterization techniques, such as electron energy loss spectrometry (EELS) in the transmission electron microscope (TEM), neutron and X-ray scattering, optical microscopy and vibrational spectroscopy, are used to understand the charge storage mechanisms¹².

¹A. J. Drexel Nanomaterials Institute, and Department of Materials Science and Engineering, Drexel University, Philadelphia, PA, USA. ²Storage of Electrochemical Energy (SEE), Department of Radiation Science and Technology, Delft University of Technology, Delft, The Netherlands. ³These authors contributed equally: Danzhen Zhang, Ruocun (John) Wang. ✉e-mail: x.wang-22@tudelft.nl; gogotsi@drexel.edu

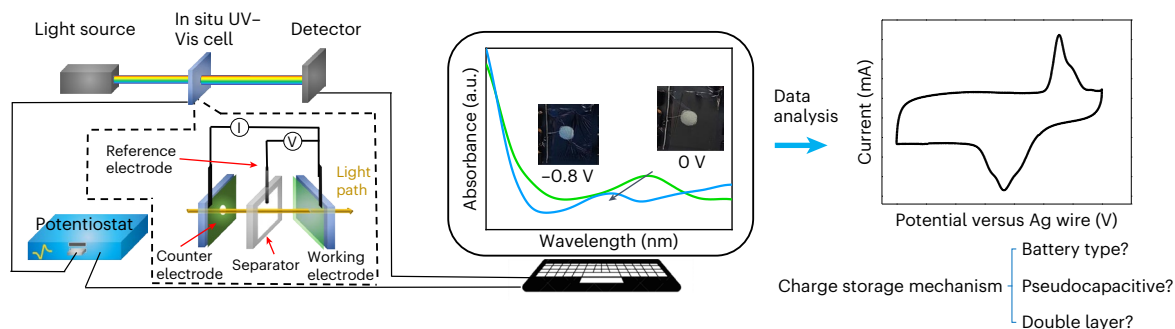


Fig. 1 The setup for in situ electrochemical UV-Vis spectroscopy. A simple three-electrode in situ UV-Vis cell is designed to allow electrochemical characterization with simultaneous recording of UV-Vis absorption spectra. Analysis of the UV-Vis data allows one to distinguish intercalation-based battery-

type, pseudocapacitive and EDL mechanisms. The digital photographs and UV-Vis spectra in the middle panel show the colour change of a $\text{Ti}_3\text{C}_2\text{T}_x$ electrode in $1\text{ M H}_2\text{SO}_4$ at -0.8 V and 0 V versus Ag wire.

In particular, scanning transmission electron microscopy/EELS with unparalleled spatial resolution were used to characterize the structural reconstruction at the surface of cathode materials in lithium-ion batteries¹³. X-ray-based in situ/operando techniques such as X-ray absorption spectroscopy (XAS), X-ray diffraction (XRD), and X-ray photoelectron spectroscopy have been used to quantitatively monitor changes in oxidation state, lattice parameters, and crystal and electronic structure of electrode materials^{10,14–17}. In situ/operando vibrational spectroscopy, such as Raman and infra-red spectroscopy, were also used to provide information about the charge storage mechanism and intercalation of ions^{18,19}. For example, in situ XAS, Raman and XRD were used to determine the charge storage mechanism of $\text{Ti}_3\text{C}_2\text{T}_x$ MXene in H_2SO_4 electrolyte, showing a change in the oxidation state of Ti caused by the charge transfer from H^+ to =O terminations, forming $-\text{OH}$ (refs. 17,20). However, all the above techniques have limitations, including instrument cost and accessibility. TEM/EELS suffers from limited choices of materials due to high-vacuum environments and radiation damage from the electron beam²¹. XAS typically requires access to synchrotron facilities, thus being costly and time intensive²². The reflection and absorption of X-rays by the substrate and cell materials may affect the acquired XRD and XAS data quality²³. Raman spectroscopy is a versatile optical characterization tool that gives information about chemical changes during cycling, but not all materials have distinct Raman peaks, and quantifying the data is challenging¹¹.

Among other techniques, optical microscopy and ultraviolet-visible (UV-Vis) spectroscopy have been combined with in situ electrochemical techniques, namely electro-optical imaging and spectroelectrochemistry, and have contributed to the elucidation of electrochromic properties and charge storage mechanisms^{24–29}. Dark-field microscopy has been used to monitor the growth and under-potential deposition of nanoparticles. The time derivative of optical signals, such as scattered light intensity change and wavelength shift, could be reconstructed into optical 'CVs' or opto-voltammogram, which resembled the electrochemical CVs^{30,31}. Other optical microscopy techniques, such as optical interferometric scattering microscopy²⁶, fluorescence-enabled electrochemical microscopy³² and surface plasmon resonance microscopy³³, also enabled mechanistic studies of battery and electrocatalytic materials. When it comes to the studies of pseudocapacitive materials, analysis of optical density was used to distinguish diffusion-limited and pseudocapacitive behaviours in hexagonal WO_3 and Prussian Blue (PB) nanoparticles^{34,35}. While electro-optical imaging is powerful in deciphering the nanoscale electrochemical behaviour of materials, it may require advanced computer-assisted analysis, a long time to collect enough statistics, and instrumental modifications that are possible only in specialized labs. In contrast, in situ electrochemical UV-Vis spectra come directly

from the instrument, contain statistical information from a large area and do not require modifications of the instrument. It is a widespread technique for studying the electrochromic behaviour of materials. In situ differential UV-Vis transmission spectra showed different colouration efficiencies for different redox couples in monoclinic WO_3 (ref. 36). Milliron et al. distinguished the electrochromic switching kinetics, including capacitive charging, surface redox and ion insertion in metal oxide nanocrystals by comparing spectroelectrochemical features³⁷. However, certain effects like optical response activated by localized surface plasmon resonance are specific to nanocrystals. In energy storage, Balland et al. used spectroelectrochemical analysis to study charge storage mechanisms in MnO_2 and anatase TiO_2 and brought unique insights on the electrodeposition/dissolution of manganese species and the role of proton in the presence of other cations in aqueous electrolytes^{25,38,39}. There are also studies on using UV-Vis spectroscopy to quantify the polysulfide absorption during charging/discharging processes and using UV-Vis spectroelectrochemistry for elucidating the peculiarities of the mechanisms in switching process during electrochemical or chemical processes^{24,40}. Valurouthu et al. observed surface-redox-caused electrochromic effects in titanium-based MXenes⁴¹. These studies demonstrate in situ UV-Vis spectroscopy as a powerful tool for studying charge storage mechanisms. However, the existing studies mainly focused on using UV-Vis spectroscopy to investigate specific charge storage mechanisms (which, where and how ions are stored). Herein, we extend this technique as a generic method for distinguishing intercalation-based battery-type, surface redox and EDL processes and providing quantitative insights into the charge storage mechanisms.

In this article, we introduce in situ UV-Vis spectroscopy (Fig. 1, details in Supplementary Fig. 1 and Methods) for monitoring redox activities in electrochemical systems. Compared with conventional methods for studying oxidation state changes of materials, UV-Vis spectroscopy is affordable, accessible, high-speed and non-destructive¹¹. The cost of UV-Vis spectrometers is an order of magnitude lower than Raman spectrometers and about two orders of magnitude lower than TEMs. We investigated five electrochemical systems and used multiple potential step chronoamperometry (MUSCA) and CV methods in combination with in situ UV-Vis spectroscopy for determining energy storage mechanisms. MUSCA method minimizes ohmic polarization and allows us to measure wide-range UV-Vis spectra at individual fixed potential steps, providing more spectroscopic information on the evolution of the electronic structure of materials⁴². The CV method offers operando tracking of absorbance change at a fixed wavelength, giving more precise kinetic information. Electrochemical charge storage mechanisms were distinguished and interpreted with quantitative analyses of the UV-Vis spectra.

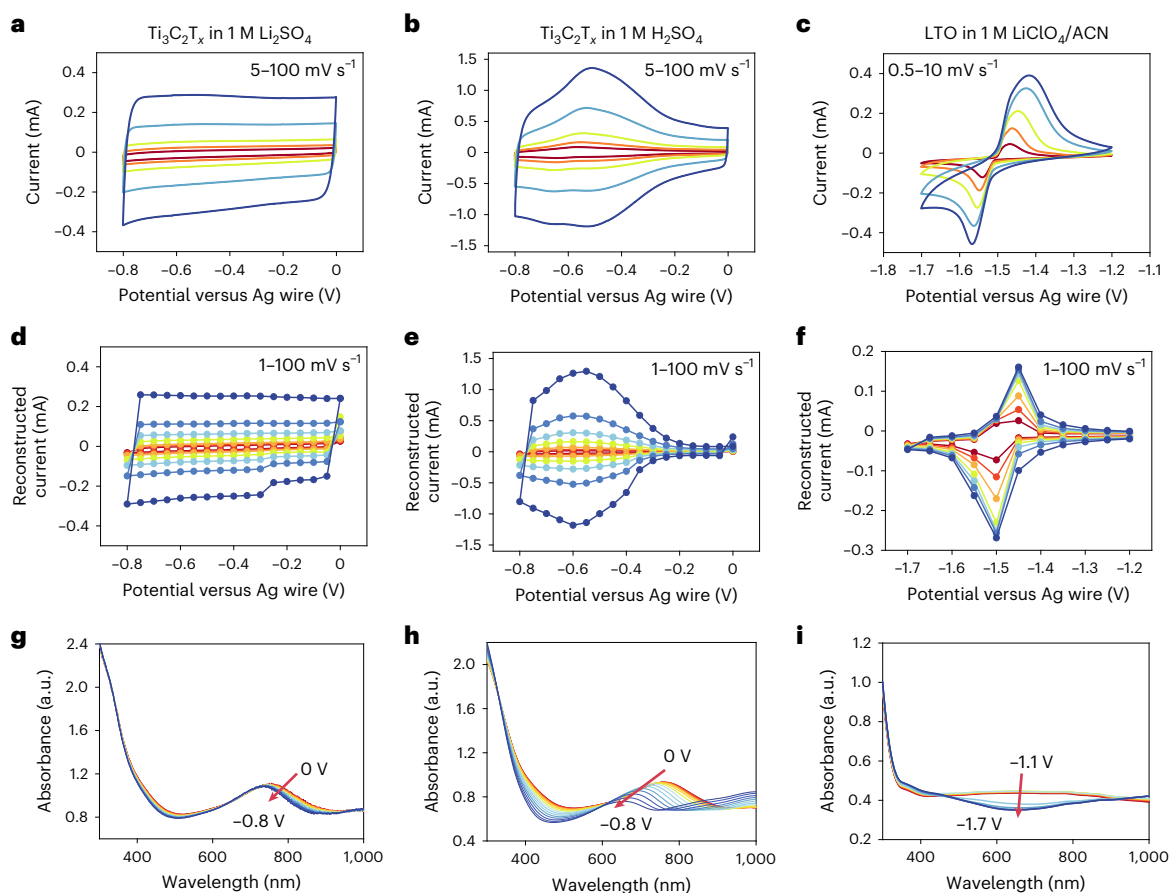


Fig. 2 | Electrochemical CV curves, reconstructed CV curves and in situ electrochemical UV-Vis spectra. **a–c**, CV curves of the in situ UV-Vis cells at different scan rates of $\text{Ti}_3\text{C}_2\text{T}_x$ in 1 M Li_2SO_4 (from inner to outer: 5, 10, 20, 50 and 100 mV s^{-1}) (**a**), $\text{Ti}_3\text{C}_2\text{T}_x$ in 1 M H_2SO_4 (from inner to outer: 5, 10, 20, 50 and 100 mV s^{-1}) (**b**) and lithium titanate (LTO) in 1 M $\text{LiClO}_4/\text{ACN}$ (from inner to outer:

0.5, 1, 2, 5 and 10 mV s^{-1}) (**c**). **d–f**, Reconstructed CV curves from MUSCA data (from inner to outer: 1, 2, 4, 10, 20, 40 and 100 mV s^{-1}) of $\text{Ti}_3\text{C}_2\text{T}_x$ in 1 M Li_2SO_4 (**d**), $\text{Ti}_3\text{C}_2\text{T}_x$ in 1 M H_2SO_4 (**e**) and LTO in 1 M $\text{LiClO}_4/\text{ACN}$ (**f**). **g–i**, In situ UV-Vis absorption spectra of $\text{Ti}_3\text{C}_2\text{T}_x$ in 1 M Li_2SO_4 (**g**), $\text{Ti}_3\text{C}_2\text{T}_x$ in 1 M H_2SO_4 (**h**) and LTO in 1 M $\text{LiClO}_4/\text{ACN}$ (**i**) in the cathodic cycles.

Electrochemistry of the in situ UV-Vis cells

To demonstrate the wide applicability of in situ UV-Vis spectroscopy, we selected three electrode–electrolyte systems to represent the three categories of electrochemical energy storage processes, namely $\text{Ti}_3\text{C}_2\text{T}_x$ in 1 M Li_2SO_4 aqueous electrolyte for EDL capacitance⁴³, $\text{Ti}_3\text{C}_2\text{T}_x$ in 1 M H_2SO_4 aqueous electrolyte for pseudocapacitance²⁰ and $\text{Li}_4\text{Ti}_5\text{O}_{12}$ (LTO) in 1 M LiClO_4 in acetonitrile (ACN) electrolyte for intercalation-based battery-type redox⁴⁴. Basic physical characterizations of these materials are shown in Supplementary Fig. 2.

CV has been considered a practical method to determine the dominating charge storage mechanism of electrodes. We performed CV on the aforementioned electrochemical systems in the in situ UV-Vis cells shown in Fig. 2a–c. The CV curves of $\text{Ti}_3\text{C}_2\text{T}_x$ in 1 M Li_2SO_4 are almost rectangular at scan rates from 5 to 100 mV s^{-1} (Fig. 2a). Meanwhile, $\text{Ti}_3\text{C}_2\text{T}_x$ in 1 M H_2SO_4 shows a pair of broad peaks at $\sim\pm 0.5$ V versus Ag on the anodic and cathodic branches of the CV curves (Fig. 2b). The CV curves of $\text{Ti}_3\text{C}_2\text{T}_x$ MXene in the neutral and acidic aqueous electrolytes are consistent with the literature^{20,43}. The $\text{Ti}_3\text{C}_2\text{T}_x$ in 1 M Li_2SO_4 system is dominated by the EDL formation, whereas protonation leads to charge transfer in the $\text{Ti}_3\text{C}_2\text{T}_x$ in 1 M H_2SO_4 system. The charge storage mechanism of the latter has been validated by in situ X-ray absorption previously¹⁷. LTO in 1 M $\text{LiClO}_4/\text{ACN}$ shows a typical battery-type CV curve with a pair of sharp peaks with large separations (Fig. 2c). The sharp peaks in the CV curves correspond to a nucleation-controlled Faradaic reaction that involves phase transformation during Li^+ intercalation⁴⁵.

To distinguish between diffusion and surface-controlled charge storage mechanisms, we evaluated the kinetic limitations in the three systems with b value analysis by solving the relation between peak current and scan rate according to

$$i_p = av^b \quad (1)$$

where v is scan rate, i_p is peak current, and a and b are constants. b values are determined by calculating the slope of $\log(i_p)$ and $\log(v)$ as shown in Supplementary Fig. 3. b values provide important insight into kinetic limitations: $b = 1$ represents surface-controlled processes, and $b = 0.5$ indicates diffusion- or nucleation-controlled processes⁴⁶. Here the b values of $\text{Ti}_3\text{C}_2\text{T}_x$ in 1 M H_2SO_4 and $\text{Ti}_3\text{C}_2\text{T}_x$ in 1 M Li_2SO_4 were determined to be 0.921 and 0.916, on the basis of the CV curves at scan rates from 5 mV s^{-1} to 100 mV s^{-1} , which indicated the surface-controlled kinetics of the processes. Meanwhile, the b value of LTO in 1 M $\text{LiClO}_4/\text{ACN}$ was determined to be 0.499 (Supplementary Fig. 3), agreeing with the nucleation-controlled process. Hence, the b value of all three systems agrees with the charge storage mechanism based on the shape of CV curves and validates that the in situ UV-Vis cells can provide a proper electrochemical characterization of the systems.

Distinguishing charge storage mechanisms

To acquire full absorption spectra in the UV-Vis range, the MUSCA method (details are provided in Methods) was first used to build a correlation between electrochemical behaviour and in situ UV-Vis spectra.

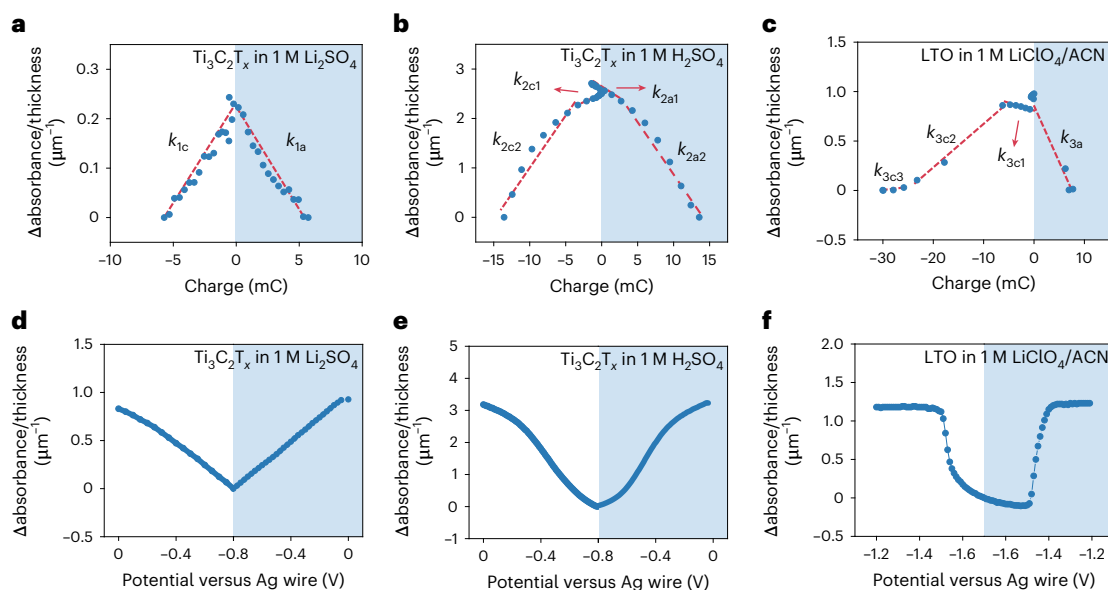


Fig. 3 | Correlation between in situ UV-Vis spectra and electrochemical results. **a–c**, Relative absorbance change (Δ absorbance/thickness) versus charge of $\text{Ti}_3\text{C}_2\text{T}_x$ in 1 M Li_2SO_4 (**a**), $\text{Ti}_3\text{C}_2\text{T}_x$ in 1 M H_2SO_4 (**b**) and lithium titanate (LTO) in 1 M $\text{LiClO}_4/\text{ACN}$ electrolyte (**c**) with MUSCA method. k_c is the cathodic slope and k_a is the anodic slope, respectively. For $\text{Ti}_3\text{C}_2\text{T}_x$ in 1 M H_2SO_4 , the two linear fittings are separated by the starting point (-0.35 V) of pseudocapacitive peaks at the reconstructed CV curves shown in Fig. 2e. For LTO in 1 M $\text{LiClO}_4/$

ACN, three linear fittings in the cathodic cycle are separated by the peaks at the reconstructed CV curves shown in Fig. 2f. The linear fitting results are presented in Supplementary Table 1. **d–f**, Relative absorbance change versus potential dependencies of $\text{Ti}_3\text{C}_2\text{T}_x$ in 1 M Li_2SO_4 (**d**), $\text{Ti}_3\text{C}_2\text{T}_x$ in 1 M H_2SO_4 (**e**) and LTO in 1 M $\text{LiClO}_4/\text{ACN}$ electrolyte (**f**) recorded using the CV method. The blue-shadowed regions represent the anodic cycles.

MUSCA allows for the reconstruction of CV curves with a potential step of 50 mV shown in Fig. 2d–f, which resemble the original electrochemical CV curves in this case (details of CV curves reconstruction are provided in Methods). The spectra during the cathodic cycles are shown in Fig. 2g–i, and the spectra of the anodic cycle are given in Supplementary Fig. 4, showing excellent reversibility. During the CV experiment, a change from the original green colour of MXene to blue colour in the electrochemically reduced state was observed (middle panel in Fig. 1). The UV-Vis absorption spectrum of pristine $\text{Ti}_3\text{C}_2\text{T}_x$ MXene shows a transverse surface plasmon resonance peak at ~ 780 nm (ref. 47). The plasmonic peak of the $\text{Ti}_3\text{C}_2\text{T}_x$ electrode in 1 M Li_2SO_4 shows a downshift from 770 nm to 740 nm when scanning from 0 V to -0.8 V. Meanwhile, the UV-Vis spectra of $\text{Ti}_3\text{C}_2\text{T}_x$ in 1 M H_2SO_4 have a much larger downshift of the plasmonic peak to ~ 650 nm over the same potential window. The more notable shift of the plasmon resonance peak in the acidic aqueous electrolyte is attributed to the protonation of surface terminations of $\text{Ti}_3\text{C}_2\text{T}_x$, a pseudocapacitive process⁴⁸.

The UV-Vis spectra of pristine LTO show no apparent peaks in the visible range⁴⁹. When the potential drops from -1.2 V to -1.5 V versus Ag, the UV-Vis spectra show almost no change. However, a valley in the absorption spectrum (Fig. 2i) at 650 nm emerges abruptly at -1.55 V versus Ag, corresponding to the peak position in CV curves of the LTO. The absorbance of this peak decreases as the potential further drops to -1.7 V. The abrupt change corresponds to the phase transformation between defective spinel $\text{Li}_4\text{Ti}_5\text{O}_{12}$ and rock-salt $\text{Li}_7\text{Ti}_5\text{O}_{12}$ structure during the lithium-ion (de)intercalation⁵⁰. The absorbance changes in the UV-Vis spectra at the signature wavelengths were only 0.020 for $\text{Ti}_3\text{C}_2\text{T}_x$ in 1 M Li_2SO_4 , 0.175 for $\text{Ti}_3\text{C}_2\text{T}_x$ in 1 M H_2SO_4 and around 0.090 but with the abrupt change for LTO in 1 M $\text{LiClO}_4/\text{ACN}$ electrolyte. Due to the dependence of absorbance on the electrode thickness, we performed a series of analyses of thickness and UV-Vis absorbance derivative, which are shown in Supplementary Figs. 5 and 6 and discussed in Supplementary Note 1, to subtract the effects of thickness on the absolute absorbance values. Thus, the following absorbance values are normalized by thickness.

To quantify the relationship between absorbance and charge storage, we plotted in Fig. 3 the relative absorbance change versus the charge of these three systems based on the in situ UV-Vis spectra collected with the MUSCA method (details of relative absorbance change and charge calculations are provided in Supplementary Notes 2 and 3, respectively). For $\text{Ti}_3\text{C}_2\text{T}_x$, we chose the wavelength corresponding to the plasmonic peak, as its absorbance has been found to correlate with the Ti oxidation state change⁴⁸. Since the absorbance of LTO does not have a signature wavelength in the UV-Vis range, we used 650 nm for this analysis as this wavelength corresponds to the most substantial absorbance change during the electrochemical cycling. Quantification reveals different relations between absorbance change and charge stored in the three systems. For $\text{Ti}_3\text{C}_2\text{T}_x$ in 1 M Li_2SO_4 , the absorbance change with charge is almost linear, and there is no difference between the cathodic and the anodic cycles (Fig. 3a). For $\text{Ti}_3\text{C}_2\text{T}_x$ in 1 M H_2SO_4 , there are two linear slopes corresponding to the EDL and pseudocapacitive charging, respectively. k_{2c1} and k_{2a1} represent two EDL charging processes in a relatively wide potential range, while k_{2a2} and k_{2c2} represent the pseudocapacitive surface redox reactions. For LTO in 1 M $\text{LiClO}_4/\text{ACN}$, there are three slope stages, particularly distinct in the cathodic cycle (Fig. 3c). The different stages of linear fitting also demonstrated the consistency between UV-Vis absorbance change and the electrochemical charge process. The apparently larger changes of charge and absorbance for k_{3c2} stage result from the redox reaction of LTO, while the other two stages are dominated by the EDL charge storage. Due to the phase transformation happening in a very narrow potential window, the 50 mV potential steps could not adequately present the redox peak, and we introduced the CV method (details of the CV method are provided in Methods) to achieve higher resolution. Overall, in all three systems, relative absorbance changes show a good correlation with charge within different electrochemical reaction stages.

The difference between battery-type, surface redox and EDL charge storage processes can be distinguished by analysing the slope

of relative absorbance change versus potential plots and by calculating the derivatives ratio. Calculating the relative absorbance change eliminates the effects of thickness and potentials. The change rate can give us information on how to distinguish between different charge mechanisms. The relative absorbance change versus potential is plotted in Fig. 3d–f. The differences between the three typical electrochemical processes are evident in terms of the slope and shape of the curves (Supplementary Fig. 7a). For the EDL-dominated case of $\text{Ti}_3\text{C}_2\text{T}_x$ in 1 M Li_2SO_4 , an almost linear relative absorbance change was obtained from -0.8 V to 0 V, with a slope of $-1.06 \text{ V}^{-1} \mu\text{m}^{-1}$ as shown in Fig. 3d. A more notable relative absorbance change can also be observed in $\text{Ti}_3\text{C}_2\text{T}_x$ in 1 M H_2SO_4 at the potential of surface redox reaction. The slope at -0.50 V is $-5.78 \text{ V}^{-1} \mu\text{m}^{-1}$, which is about five times larger than the EDL system (the same material in the neutral electrolyte). The relative absorbance change of the battery system has hysteresis and abrupt changes, especially at the potential where the phase transformation occurs. The calculated slope of the LTO in 1 M $\text{LiClO}_4/\text{ACN}$ system around the CV peak position of -1.52 V is $-16.22 \text{ V}^{-1} \mu\text{m}^{-1}$, which is three times larger than that in the pseudocapacitive system as the surface redox reaction happens over a narrower range of potentials. However, the selection of the wavelength may affect the absolute values of the slope. To address this issue, derivative ratios (detailed in Supplementary Note 2 and discussed in next section) were introduced and used to distinguish the charge storage mechanisms, additionally.

Coupling between charge transfer and UV–Vis spectral changes

Since current (i) is the rate of change of charge (Q), which can be expressed as dQ/dt , the good linearity between charge and relative absorbance change led us to take the derivative of absorbance at signature wavelengths, called normalized derivative (details of theoretical analysis and normalized derivative are provided in Supplementary Note 4), collected with the MUSCA method. The normalized derivative is then plotted as a function of potential for both cathodic and anodic scans and compared to electrochemical CV curves in Supplementary Fig. 8a–c. The normalized derivative plots closely resemble electrochemical CV curves in all these three systems, leading us to name this data representation as the UV–Vis CV curve. In general, the shape of the UV–Vis CV curve resembles the electrochemical CV curve for all these three systems and suggests that UV–Vis spectroscopy can be used to monitor electrochemical charge storage processes. $\text{Ti}_3\text{C}_2\text{T}_x$ in 1 M Li_2SO_4 has small derivative values around $1.0 \text{ V}^{-1} \mu\text{m}^{-1}$ at all potentials (Supplementary Fig. 8a). For the $\text{Ti}_3\text{C}_2\text{T}_x$ in 1 M H_2SO_4 system, the derivative value is also negligible at the EDL charging region in the electrochemical CV curve (Supplementary Fig. 8b). However, the derivative value started to increase at the onset potential of the surface redox reaction and reached the maximum value at the peak potential of the electrochemical CV curve in the cathodic cycle. For the LTO in 1 M $\text{LiClO}_4/\text{ACN}$, the derivative has values near 0 at the initial stage and increases abruptly when the redox reaction occurs at -1.55 V (Supplementary Fig. 8c). We note that, in certain cases, the peak of UV–Vis CV curves obtained with the MUSCA method emerged at a slightly more positive potential compared with the electrochemical CV curve. This is probably due to the insufficient data points collected in the potential range of the redox peak. Therefore, we utilized single wavelength absorbance acquisition while using CV to operate the in situ UV–Vis cell (CV method) to obtain more precise UV–Vis CV curves.

The UV–Vis CV curves with higher precision (every 10 mV) are plotted in Fig. 4a–c with blue colour. As the signature wavelengths, 450 nm and 650 nm were selected for $\text{Ti}_3\text{C}_2\text{T}_x$ and LTO, respectively, since these wavelengths showed the largest absorbance change. In this case, the proportionality between absorbance and charge of the LTO system becomes closer to linear, as shown in Supplementary Fig. 9 and discussed in Supplementary Note 5. The CV method-derived UV–Vis CV curves closely resemble their corresponding electrochemical CV curves (Fig. 4–c) in terms of the shape, the onset potential of

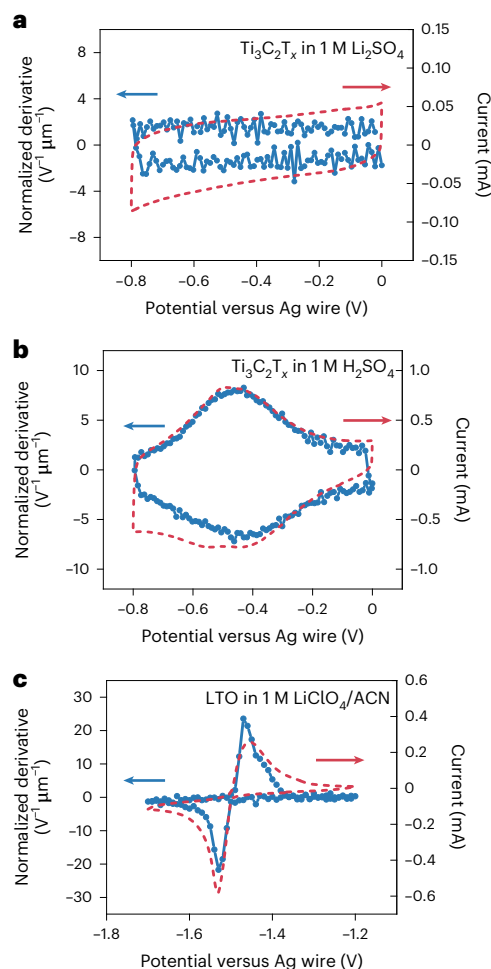


Fig. 4 | Comparison of electrochemical and UV–Vis CV curves of selected electrochemical systems collected using the CV method. **a**, Electrochemical (red) and UV–Vis CV (blue) curves of $\text{Ti}_3\text{C}_2\text{T}_x$ in 1 M Li_2SO_4 at 10 mV s^{-1} . **b**, Electrochemical (red) and UV–Vis CV (blue) curves of $\text{Ti}_3\text{C}_2\text{T}_x$ in 1 M H_2SO_4 at 10 mV s^{-1} . **c**, Electrochemical (red) and UV–Vis CV (blue) curves of lithium titanate (LTO) in 1 M $\text{LiClO}_4/\text{ACN}$ at 1 mV s^{-1} . The signature wavelengths used for UV–Vis CV curves are 450 nm for $\text{Ti}_3\text{C}_2\text{T}_x$ and 650 nm for LTO.

the peaks, and the peak potential. The match between the UV–Vis and electrochemical CV curves illustrates that the UV–Vis absorbance change of electrode material is highly responsive towards the change in the state of charge.

To show that this method is not limited to Ti redox, we conducted in situ UV–Vis analysis on PB, a battery-type material with electrochromic characteristics, in 1 M KCl electrolyte^{51,52}. As shown in Supplementary Fig. 10a,b, the absorbance decreased within the cathodic process, and a reversible change occurred in the anodic cycle. It should be noticed that there was an abrupt change in the spectra at the CV curve peaks. Then, the normalized derivative at a fixed wavelength (700 nm) was calculated using MUSCA and CV methods, as shown in Supplementary Fig. 10d,e. Both UV–Vis CV curves are similar to the electrochemical CV curve and show a larger normalized derivative value when the electrochemical CV curve shows peaks. Similarly, the CV method-derived UV–Vis CV curve fits better with the electrochemical CV curve than the MUSCA UV–Vis CV curve. Hence, the correlation between the UV–Vis spectra and the electrochemical process is general and can be widely applicable to materials that experience changes in the electronic structure upon charge storage, such as conducting polymers and ceramics.

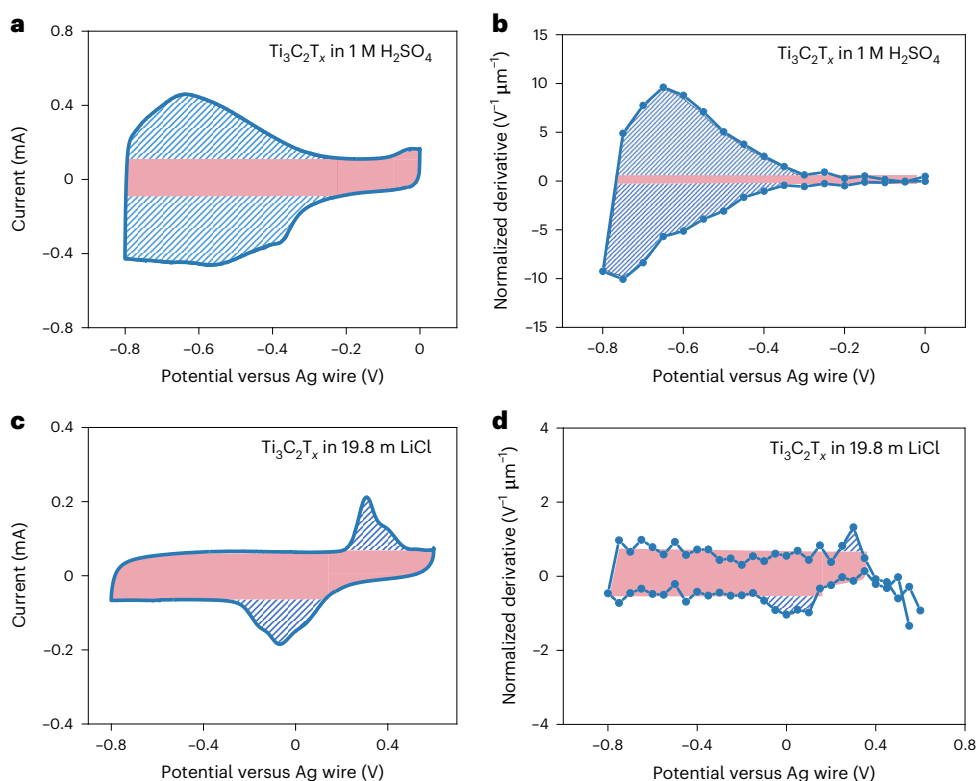


Fig. 5 | EDL and surface redox contributions to the total charge for $\text{Ti}_3\text{C}_2\text{T}_x$ in different electrolytes. a, c, CV curves at 20 mV s^{-1} for $\text{Ti}_3\text{C}_2\text{T}_x$ in $1 \text{ M H}_2\text{SO}_4$ (a) and $\text{Ti}_3\text{C}_2\text{T}_x$ in 19.8 m LiCl (c). b, d, Normalized derivative versus potential collected

with MUSCA method for $\text{Ti}_3\text{C}_2\text{T}_x$ in $1 \text{ M H}_2\text{SO}_4$ (b) and 19.8 m LiCl (d). The pink region indicates the EDL contribution during the charge process (details in Supplementary Note 7).

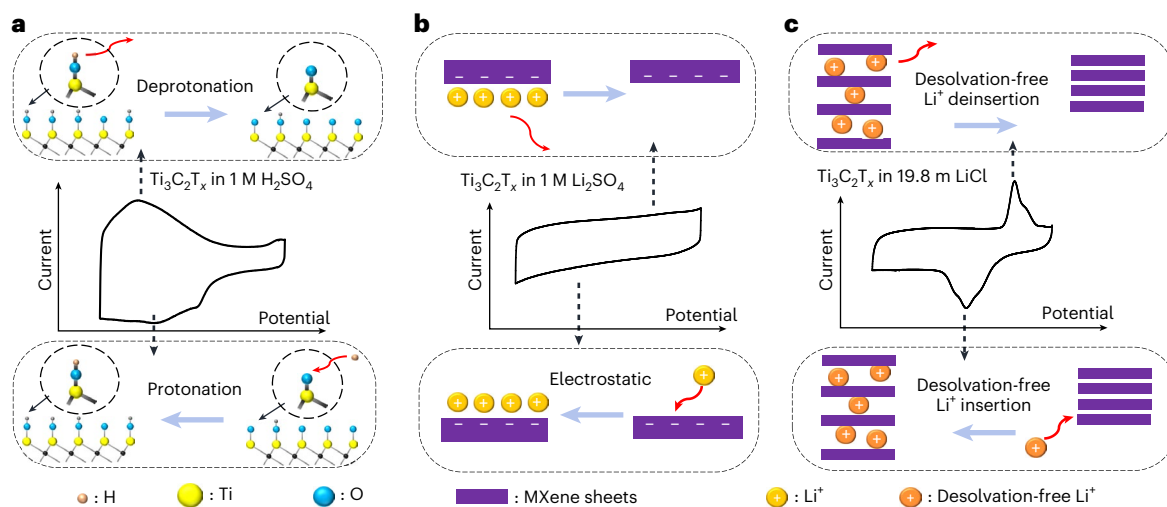


Fig. 6 | Schematic illustrating the difference of mechanisms of charge storage by $\text{Ti}_3\text{C}_2\text{T}_x$ in different electrolytes. a, In the cathodic (bottom) and anodic (top) processes, the protonation/deprotonation dominates the charge storage of $\text{Ti}_3\text{C}_2\text{T}_x$ in $1 \text{ M H}_2\text{SO}_4$. b, In the cathodic (bottom) and anodic (top) processes, the

EDL formation dominates the charge storage mechanism of $\text{Ti}_3\text{C}_2\text{T}_x$ in $1 \text{ M Li}_2\text{SO}_4$. c, In the cathodic (bottom) and anodic (top) processes, the desolvation-free lithium ion insertion/desertion leads to the peaks in the CV curve for $\text{Ti}_3\text{C}_2\text{T}_x$ in 19.8 m LiCl .

It is known that the UV–Vis absorbance change is caused by the change in the oxidation state of the electrode material⁵³. For example, the oxidation state of the metal oxides (such as WO_3 (ref. 54) and TiO_2 (ref. 55)) correlates with the colour change. The similarity between the UV–Vis and electrochemical CV curves confirms that the changing rate of the absorbance is higher for the electrochemical reactions

that involve Faradaic charge transfer. Furthermore, the calculated derivative ratios shown in Supplementary Fig. 7b showcase the distinctive differences among the various charge storage mechanisms. For example, the derivative ratios are -54 for LTO in $\text{LiClO}_4/\text{ACN}$ and -51 for the PB in 1 M KCl , both involving battery-type Faradaic reactions. They are substantially greater than that of pseudocapacitive $\text{Ti}_3\text{C}_2\text{T}_x$ in 1 M

H_2SO_4 (-10) and the EDL capacitive $\text{Ti}_3\text{C}_2\text{T}_x$ in 1 M Li_2SO_4 (-1.0). It agrees with the fact that the Faradaic reaction leads to a larger oxidation state change in the battery-type electrode within a narrow potential window compared with a pseudocapacitive or an EDL capacitive electrode.

A quantitative correlation was established in Supplementary Note 4 between the absorbance change, number of charge transfer, n , and extinction coefficients, which allows us to calculate the oxidation state changes, similar to in situ XAS:

$$n = \frac{l(\varepsilon_{\text{ox}} - \varepsilon_{\text{re}})}{\tau^0 F} \times \frac{\Delta Q}{\Delta A} \quad (2)$$

where l is thickness of the film, ε_{ox} and ε_{re} are the extinction coefficients of the material in the oxidized state and the reduced state, respectively, τ^0 is the total molar amount of electrode material, F is Faraday constant, and ΔQ and ΔA are the charge difference and absorbance change, respectively, within a selected time interval or potential range.

Here we calculated oxidation state change for $\text{Ti}_3\text{C}_2\text{T}_x$ in 1 M H_2SO_4 . As detailed in Supplementary Note 6, we obtained the extinction coefficients by performing in situ UV-Vis analysis with the MUSCA method on multiple films of different thicknesses. The calculated number of electrons transferred during the pseudocapacitive process is 0.442 per $\text{Ti}_3\text{C}_2\text{T}_x$ unit, which is equivalent to 0.147 electrons per Ti atom, close to the 0.134 electrons per Ti atom obtained from in situ XAS⁵⁶. This calculation further demonstrates the potential of UV-Vis to compete with XAS.

Understanding an unconventional electrochemical system

$\text{Ti}_3\text{C}_2\text{T}_x$ in 19.8 m LiCl shows well-defined peaks in the CV curves. This phenomenon is unconventional due to the non-Faradaic nature of these peaks¹⁰. Herein, we use in situ UV-Vis to evaluate the Faradaic contribution during the process. As seen in Supplementary Fig. 12a, the plasmonic peak of $\text{Ti}_3\text{C}_2\text{T}_x$ in 19.8 m LiCl shifts around 65 nm, which is smaller than that in 1 M H_2SO_4 (130 nm), but larger than that in 1 M Li_2SO_4 (30 nm). Similarly, Supplementary Fig. 7 shows that the derivative ratio (-1.4) of $\text{Ti}_3\text{C}_2\text{T}_x$ in 19.8 m LiCl also falls between the derivative ratios in H_2SO_4 (-10) and the Li_2SO_4 (-1.0), but is closer to the Li_2SO_4 electrolyte. Peaks also exist in the UV-Vis CVs (Supplementary Fig. 12d,e), but are still small compared with $\text{Ti}_3\text{C}_2\text{T}_x$ in 1 M H_2SO_4 . These observations support the hypothesis that charge storage in $\text{Ti}_3\text{C}_2\text{T}_x$ in 19.8 m LiCl is dominated by the EDL mechanism with minor Faradaic contributions.

We further compare current and normalized derivative value of $\text{Ti}_3\text{C}_2\text{T}_x$ in different electrolytes to determine the charge storage mechanism of $\text{Ti}_3\text{C}_2\text{T}_x$ in 19.8 m LiCl. As detailed in Supplementary Note 7, we assume the contribution of EDL during the charging/discharging process is consistent throughout the potential window if the surface does not change substantially. In electrochemical CV curves, we represent the EDL contributed current as the pink rectangular regions in Fig. 5a,c. The blue-shaded regions in Fig. 5a represent the redox contributed current, while the blue-shaded regions in Fig. 5c represent the to-be-determined charge storage beyond EDL contribution. We performed the same treatment for UV-Vis CV curves in Fig. 5b,d by assuming the normalized derivative contributed by EDL remains constant. We have determined earlier that the absorbance contribution from a certain amount of charge storage remains constant under the same mechanism. Hence, we can determine the charge storage mechanism by comparing the ratio of absorbance change in the shaded areas to the EDL contributed absorbance change. We show in Supplementary Note 7 that this is equivalent to comparing the average normalized derivative in the shaded area to the EDL contributed normalized derivative. Herein, the average redox-contributed normalized derivative for $\text{Ti}_3\text{C}_2\text{T}_x$ in 1 M H_2SO_4 is $5.54 \text{ V}^{-1} \mu\text{m}^{-1}$, greater than the EDL-contributed normalized derivatives of $0.58 \text{ V}^{-1} \mu\text{m}^{-1}$, which confirms the redox-contributed normalized derivatives are far more than EDL-contributed normalized derivative. On the other hand, the

average normalized derivative for the blue-shaded area of $\text{Ti}_3\text{C}_2\text{T}_x$ in 19.8 m LiCl is $0.25 \text{ V}^{-1} \mu\text{m}^{-1}$, which is smaller than the EDL-contributed normalized derivative of $0.62 \text{ V}^{-1} \mu\text{m}^{-1}$. This indicates that the unknown mechanism in the blue-shaded region in Fig. 5d is similar to EDL mechanism and is unlikely to involve redox processes.

The charge storage mechanisms of $\text{Ti}_3\text{C}_2\text{T}_x$ in different electrolytes are discussed below. In the case of $\text{Ti}_3\text{C}_2\text{T}_x$ in 1 M H_2SO_4 , proton intercalation is accompanied by the oxidation state change of Ti. This is due to the surface redox reaction when the intercalated protons bond to the =O groups on the surface of $\text{Ti}_3\text{C}_2\text{T}_x$. In this case, the surface redox reactions contribute additional charge storage, leading to the peaks observed in the electrochemical CV curve as shown in Fig. 6a. On the other hand, in 1 M Li_2SO_4 , there are no redox reactions, and the inserted Li^+ form EDLs in the interlayer, as shown in Fig. 6b. Thus, a linear relationship between time and charge forms a rectangular CV curve. Our previous study shows that the two separated peaks in the CV curves of $\text{Ti}_3\text{C}_2\text{T}_x$ in 19.8 m LiCl correspond to the desolvation-free Li^+ insertion/deinsertion¹⁰. As discussed above, the change in the oxidation state should lead to a notable change in the UV-Vis absorption spectra. The analysis from in situ UV-Vis study in this work indicates that a non-Faradaic reaction dominates the process and eliminates confusion that may be caused by the presence of the well-defined peaks in the electrochemical CV curves. Hence, the desolvation-free cation insertion/deinsertion is accompanied by negligible surface redox, and the peaks in the CV curve should be due to a large number of ions inserted and deinserted at the peak potentials, forming EDL between MXene sheets (Fig. 6c; water is not shown).

Conclusions

We have demonstrated that in situ UV-Vis spectroscopy is a powerful technique for determining charge storage mechanisms and monitoring redox processes in various electrochemical systems. Using the UV-Vis absorbance derivative, we show a correlation between spectral changes and electrochemical processes, which allows us to distinguish between the EDL, pseudocapacitive and intercalation-based battery-type redox processes. Proper calibration allows us to determine the number of electrons transferred quantitatively during the reaction, similar to XAS. Due to its wide accessibility and unique ability to probe electronic structure and colour change, we envision that UV-Vis will play an increasingly important role in the in situ studies of a wide range of electrochemical phenomena in materials, ranging from energy storage to SEI formation, electrolyte decomposition, electrocatalysis, electrochromism and electrochemical modulation of materials properties.

Methods

Preparation of MXene

$\text{Ti}_3\text{C}_2\text{T}_x$ was synthesized by the selective etching of Ti_3AlC_2 MAX phase powder (325 mesh) with a mixture of HF (48.5–51%, Acros Organics) and HCl (36.5–38%, Fisher Chemical) acids. Typically, 2 ml of HF, 12 ml of HCl and 6 ml of de-ionized (DI) water were mixed⁵⁷. After that, 1 g of MAX phase powder was added to the solution and stirred for 24 h at 35 °C. After etching, the reaction product was washed with DI water using a centrifuge at 2,550g for 2 min until pH >6. The obtained sediment was dispersed in a 0.5 M LiCl solution. The mixture was shaken for 15 min, and then centrifuged at 2,550g for 10 min several times until the sediment delaminated and swelled. The swelled sediment was dispersed in DI water and then centrifuged at 2,550g for 10 min. After that, the dark supernatant was collected for spray-coating.

Preparation of PB

PB was synthesized according to the Neff method on a fluorine-doped tin oxide glass (-13 Ohm per square, MSE Supplies) using the three-electrode configuration⁵⁸. Pt wire and Ag/AgCl were used as counter and reference electrodes, respectively. $\text{K}_3[\text{Fe}(\text{CN})_6]$ (10 mM), $\text{FeCl}_3 \cdot 6\text{H}_2\text{O}$ (10 mM) and KCl (50 mM) were dissolved in DI water under

stirring. The galvanostatic electrodeposition was performed using a Biologic SP150 potentiostat. A constant current (-0.05 mA, 300 s) was used to conduct electrodeposition.

Thin film preparation by spray-coating

Microscopic glass slides of $25 \times 75 \times 1$ mm (Fisher Scientific) were cleaned by sequential bath sonication (2510 Ultrasonic Cleaner, Branson) in detergent solution (Hellmanex III, Fisher Scientific) to remove the residue on the glass surface followed by immersing in DI water and ethanol for 5 min, sonication and drying with compressed air. The cleaned glass slides were plasma treated (Tergeo Plus, Pie Scientific) at 100 W with Ar/O₂ at 3/5 SCCM for 5 min to make the surface hydrophilic. The pre-treated slides were spray-coated with Ti₃C₂T_x suspension followed by air drying through a hair dryer (1875, Conair). The Ti₃C₂T_x suspension used for spray-coating has a ~ 5 mg ml⁻¹ concentration. The thickness of spray-coated films varied from ~ 50 nm to ~ 150 nm. After spray-coating, Ti₃C₂T_x films were kept in a vacuum oven overnight before performing experiments. Fluorine-doped tin oxide glass slides were treated following the same procedure as glass slides. They were spray-coated with LTO suspension to obtain thin films of around 100 nm. The LTO suspension was prepared by dispersing 1 g of LTO powder (>99%, Sigma Aldrich) in 10 ml DI water.

Material characterization

XRD patterns were measured with the Ni-filtered Cu K_α radiation ($\lambda = 1.54$ Å). Raman spectra were recorded with a Renishaw (UK) Raman InVia confocal microscope, with a laser excitation of 785 nm (for Ti₃C₂T_x) and 633 nm (for PB and LTO), grating 1,200 g mm⁻¹ and 5% laser power.

Fabrication of in situ UV-Vis spectroscopy cell

To record UV-Vis spectra of thin films, we fabricated three-electrode cells according to the procedure below. The working electrodes were Ti₃C₂T_x, LTO and PB thin films (thickness ~ 50 – ~ 150 nm) as per the last section. A silver wire was used as the reference electrode. The counter electrodes were overcapacitive films of Ti₃C₂T_x (thickness ~ 200 nm). A circular area of Ti₃C₂T_x (diameter ~ 5 mm) was removed in the middle of the counter electrode to allow the UV-Vis beam to pass through the working electrode and avoid optical contribution from the counter electrode. A thick 3 M double-sided tape (3 M VHB Tape 4910) was used to fabricate walls, which create an electrolyte reservoir attached to electrodes. We used 2 mm graphite foil (0.13 mm thick, Alfa Aesar) to provide contacts between electrodes and the potentiostat. The electrolytes used were 1 M sulfuric acid (H₂SO₄, Fisher Scientific, 98%), 19.8 m lithium chloride (LiCl, Fisher Scientific) and 1 M lithium sulfate (Li₂SO₄, Fisher Scientific). When conducting the measurements, the in situ UV-Vis cell was fixed in the middle of the sample holder to pass light through the hole of the cell.

In situ UV-Vis spectroscopy (MUSCA method and CV method)

Cells made with glass slides filled with 1 M H₂SO₄, 19.8 m LiCl, 1 M Li₂SO₄, 1 M LiClO₄/ACN and 1 M KCl were used as blanks to calibrate the system before performing in situ UV-Vis tests. The absorption spectra were recorded from 300 nm to 1,000 nm with 1 nm steps using a Thermo Scientific UV-Vis spectrometer Evolution 201 with a tungsten lamp and dual-silicon-photodiode detector. In situ UV-Vis spectra were recorded by synchronous measurements of the UV-Vis spectrophotometer with a Biologic SP 150 potentiostat (Bio-Logic). The in situ UV-Vis cell was placed on the holder of the spectrophotometer in a way that the hole in the counter electrode aligned with the beam path. Before the in situ tests, the cells were pre-cycled by performing CV at 20 mV s⁻¹ to determine the stable potential window of cells with different electrolytes (2 mV s⁻¹ for LTO). The potential windows are 0 V to -0.8 V for Ti₃C₂T_x in 1 M Li₂SO₄ and 1 M H₂SO₄, -0.8 V to 0.6 V for Ti₃C₂T_x in 19.8 m LiCl, -0.2 V to 0.6 V for PB in 1 M KCl, and -1.7 V to -1.2 V for LTO in 1 M LiClO₄/ACN,

respectively. The UV-Vis absorbance of the five electrochemical systems was recorded in situ every 50 mV from the open circuit potential to the cathodic limit potential, after the systems equilibrated at each potential step. This MUSCA technique was used to qualitatively study the kinetics of this system using the MUSCA profiles (Supplementary Fig. 14)⁴². In this in situ measurement method, the long step time (150 s for Ti₃C₂T_x and PB, and 210 s for LTO) enables the response current to level off to zero before moving to the next voltage step. After calculating the integration of current versus time, reconstructed CV curves (MUSCA CV curves) were obtained as seen in Fig. 2d–f and Supplementary Figs. 10c and 11c. For the CV method, the absorbance at a single wavelength (Ti₃C₂T_x at 450 nm, PB at 700 nm and LTO at 650 nm) was acquired using a UV-Vis spectrometer with 1 s acquisition time, when the in situ cell was running CV at a relatively low scan rate (Ti₃C₂T_x at 10 mV s⁻¹, PB at 10 mV s⁻¹ and LTO at 1 mV s⁻¹).

Reconstructed MUSCA CV curves

As shown in Supplementary Fig. 14, the resulting current was monitored as a function of time at each potential step. The mean current of first Δt at each potential step is given according to

$$\bar{i} = \frac{\int_0^{\Delta t} i dt}{\Delta t} \quad (3)$$

where Δt is the selected time and i is the response current. Then the scan rate ν is given according to

$$\nu = \frac{\Delta V}{\Delta t} \quad (4)$$

where ΔV is the potential interval (50 mV in this case). Here we selected Δt to be 0.5 s, 1.25 s, 2.5 s, 5 s, 12.5 s, 25 s and 50 s for the aforementioned five systems.

Data availability

All relevant data are available within the paper and Supplementary Information. Source data are provided with this paper.

References

- Liu, Y., Zhu, Y. & Cui, Y. Challenges and opportunities towards fast-charging battery materials. *Nat. Energy* **4**, 540–550 (2019).
- Reddy, A. L. M., Gowda, S. R., Shaijumon, M. M. & Ajayan, P. M. Hybrid nanostructures for energy storage applications. *Adv. Mater.* **24**, 5045–5064 (2012).
- Salanne, M. et al. Efficient storage mechanisms for building better supercapacitors. *Nat. Energy* **1**, 16070 (2016).
- Fleischmann, S. et al. Continuous transition from double-layer to faradaic charge storage in confined electrolytes. *Nat. Energy* **7**, 222–228 (2022).
- Boyd, S. et al. Effects of interlayer confinement and hydration on capacitive charge storage in birnessite. *Nat. Mater.* **20**, 1689–1694 (2021).
- Nikitina, V. A., Vassiliev, S. Y. & Stevenson, K. J. Metal-ion coupled electron transfer kinetics in intercalation-based transition metal oxides. *Adv. Energy Mater.* **10**, 1903933 (2020).
- Simon, P., Gogotsi, Y. & Dunn, B. Where do batteries end and supercapacitors begin? *Science* **343**, 1210–1211 (2014).
- Brousse, T., Bélanger, D. & Long, J. W. To be or not to be pseudocapacitive? *J. Electrochem. Soc.* **162**, A5185–A5189 (2015).
- Fleischmann, S. et al. Pseudocapacitance: from fundamental understanding to high power energy storage materials. *Chem. Rev.* **120**, 6738–6782 (2020).
- Wang, X. et al. Titanium carbide MXene shows an electrochemical anomaly in water-in-salt electrolytes. *ACS Nano* **15**, 15274–15284 (2021).

11. Meng, C. et al. In situ and operando characterizations of 2D materials in electrochemical energy storage devices. *Small Sci.* **1**, 2000076 (2021).
12. Lu, J., Wu, T. & Amine, K. State-of-the-art characterization techniques for advanced lithium-ion batteries. *Nat. Energy* **2**, 17011 (2017).
13. Lin, F. et al. Surface reconstruction and chemical evolution of stoichiometric layered cathode materials for lithium-ion batteries. *Nat. Commun.* **5**, 3529 (2014).
14. Liu, X. et al. Origin and regulation of oxygen redox instability in high-voltage battery cathodes. *Nat. Energy* **7**, 808–817 (2022).
15. Bagge-Hansen, M. et al. Potential-induced electronic structure changes in supercapacitor electrodes observed by in operando soft X-ray spectroscopy. *Adv. Mater.* **27**, 1512–1518 (2015).
16. Cuisinier, M. et al. Sulfur speciation in Li–S batteries determined by operando X-ray absorption spectroscopy. *J. Phys. Chem. Lett.* **4**, 3227–3232 (2013).
17. Lukatskaya, M. R. et al. Probing the mechanism of high capacitance in 2D titanium carbide using in situ X-ray absorption spectroscopy. *Adv. Energy Mater.* **5**, 1500589 (2015).
18. Richey, F. W., Dyatkin, B., Gogotsi, Y. & Elabd, Y. A. Ion dynamics in porous carbon electrodes in supercapacitors using in situ infrared spectroelectrochemistry. *J. Am. Chem. Soc.* **135**, 12818–12826 (2013).
19. Chen, D. et al. Probing the charge storage mechanism of a pseudocapacitive MnO₂ electrode using in operando Raman spectroscopy. *Chem. Mater.* **27**, 6608–6619 (2015).
20. Lukatskaya, M. R. et al. Ultra-high-rate pseudocapacitive energy storage in two-dimensional transition metal carbides. *Nat. Energy* **2**, 17105 (2017).
21. Braun, A., Kubatova, A., Wirick, S. & Mun, S. B. Radiation damage from EELS and NEXAFS in diesel soot and diesel soot extracts. *J. Electron. Spectrosc. Relat. Phenom.* **170**, 42–48 (2009).
22. Wu, Y. & Liu, N. Visualizing battery reactions and processes by using in situ and in operando microscopies. *Chem* **4**, 438–465 (2018).
23. Tripathi, A. M., Su, W.-N. & Hwang, B. J. In situ analytical techniques for battery interface analysis. *Chem. Soc. Rev.* **47**, 736–851 (2018).
24. Gribkova, O. L. & Nekrasov, A. A. Spectroelectrochemistry of electroactive polymer composite materials. *Polymers* **14**, 3201 (2022).
25. Kim, Y.-S. et al. Evidencing fast, massive, and reversible H⁺ insertion in nanostructured TiO₂ electrodes at neutral pH. Where do protons come from? *J. Phys. Chem. C* **121**, 10325–10335 (2017).
26. Merryweather, A. J. et al. Operando monitoring of single-particle kinetic state-of-charge heterogeneities and cracking in high-rate Li-ion anodes. *Nat. Mater.* **21**, 1306–1313 (2022).
27. Merryweather, A. J., Schnedermann, C., Jacquet, Q., Grey, C. P. & Rao, A. Operando optical tracking of single-particle ion dynamics in batteries. *Nature* **594**, 522–528 (2021).
28. Vaněčková, E. et al. UV/VIS spectroelectrochemistry with 3D printed electrodes. *J. Electroanal. Chem.* **857**, 113760 (2020).
29. Kaim, W. & Fiedler, J. Spectroelectrochemistry: the best of two worlds. *Chem. Soc. Rev.* **38**, 3373–3382 (2009).
30. Hu, S. et al. Observing atomic layer electrodeposition on single nanocrystals surface by dark field spectroscopy. *Nat. Commun.* **11**, 2518 (2020).
31. Brasiliense, V. et al. Opto-electrochemical in situ monitoring of the cathodic formation of single cobalt nanoparticles. *Angew. Chem. Int. Ed.* **56**, 10598–10601 (2017).
32. Guerrette, J. P., Percival, S. J. & Zhang, B. Fluorescence coupling for direct imaging of electrocatalytic heterogeneity. *J. Am. Chem. Soc.* **135**, 855–861 (2013).
33. Jiang, D. et al. Optical imaging of phase transition and Li-ion diffusion kinetics of single LiCoO₂ nanoparticles during electrochemical cycling. *J. Am. Chem. Soc.* **139**, 186–192 (2017).
34. Evans, R. C. et al. Quantifying capacitive-like and battery-like charge storage contributions using single-nanoparticle electro-optical imaging. *ChemElectroChem* **7**, 753–760 (2020).
35. Niu, B. et al. Determining the depth of surface charging layer of single Prussian blue nanoparticles with pseudocapacitive behaviors. *Nat. Commun.* **13**, 2316 (2022).
36. Darmawi, S. et al. Correlation of electrochromic properties and oxidation states in nanocrystalline tungsten trioxide. *Phys. Chem. Chem. Phys.* **17**, 15903–15911 (2015).
37. Lu, H.-C., Zydlewski, B. Z., Tandon, B., Shubert-Zuleta, S. A. & Milliron, D. J. Understanding the role of charge storage mechanisms in the electrochromic switching kinetics of metal oxide nanocrystals. *Chem. Mater.* **34**, 5621–5633 (2022).
38. Mateos, M., Makivic, N., Kim, Y.-S., Limoges, B. & Balland, V. Accessing the two-electron charge storage capacity of MnO₂ in mild aqueous electrolytes. *Adv. Energy Mater.* **10**, 2000332 (2020).
39. Kim, Y. S., Harris, K. D., Limoges, B. & Balland, V. On the unsuspected role of multivalent metal ions on the charge storage of a metal oxide electrode in mild aqueous electrolytes. *Chem. Sci.* **10**, 8752–8763 (2019).
40. Patel, M. U. & Dominko, R. Application of in operando UV/Vis spectroscopy in lithium-sulfur batteries. *ChemSusChem* **7**, 2167–2175 (2014).
41. Valurouthu, G. et al. Tunable electrochromic behavior of titanium-based MXenes. *Nanoscale* **12**, 14204–14212 (2020).
42. Shao, H., Lin, Z., Xu, K., Taberna, P.-L. & Simon, P. Electrochemical study of pseudocapacitive behavior of Ti₃C₂T_x MXene material in aqueous electrolytes. *Energy Stor. Mater.* **18**, 456–461 (2019).
43. Lukatskaya, M. R. et al. Cation intercalation and high volumetric capacitance of two-dimensional titanium carbide. *Science* **341**, 1502–1505 (2013).
44. Sun, X., Radovanovic, P. V. & Cui, B. Advances in spinel Li₄Ti₅O₁₂ anode materials for lithium-ion batteries. *N. J. Chem.* **39**, 38–63 (2015).
45. Joshi, Y., Saksena, A., Hadjixenophontos, E., Schneider, J. M. & Schmitz, G. Electrochromic behavior and phase transformation in Li_{4+x}Ti₅O₁₂ upon lithium-ion deintercalation/intercalation. *ACS Appl. Mater. Interfaces* **12**, 10616–10625 (2020).
46. Wang, J., Polleux, J., Lim, J. & Dunn, B. Pseudocapacitive contributions to electrochemical energy storage in TiO₂ (anatase) nanoparticles. *J. Phys. Chem. C* **111**, 14925–14931 (2007).
47. Maleski, K., Shuck, C. E., Fafarman, A. T. & Gogotsi, Y. The broad chromatic range of two-dimensional transition metal carbides. *Adv. Opt. Mater.* **9**, 2001563 (2020).
48. Salles, P. et al. Electrochromic effect in titanium carbide MXene thin films produced by dip-coating. *Adv. Funct. Mater.* **29**, 1809223 (2019).
49. Li, M. et al. Electrochromic properties of Li₄Ti₅O₁₂: from visible to infrared spectrum. *Appl. Phys. Lett.* **115**, 073902 (2019).
50. Scharner, S., Weppner, W. & Schmid-Beurmann, P. Evidence of two-phase formation upon lithium insertion into the Li_{1.33}Ti_{1.67}O₄ Spinel. *J. Electrochem. Soc.* **146**, 857–861 (1999).
51. Li, H. & Elezzabi, A. Y. Simultaneously enabling dynamic transparency control and electrical energy storage via electrochromism. *Nanoscale Horiz.* **5**, 691–695 (2020).
52. Peng, J. et al. Prussian blue analogues for sodium-ion batteries: past, present, and future. *Adv. Mater.* **34**, 2108384 (2022).
53. Li, R. et al. Flexible and high-performance electrochromic devices enabled by self-assembled 2D TiO₂/MXene heterostructures. *Nat. Commun.* **12**, 1587 (2021).

54. Yan, C. et al. Stretchable and wearable electrochromic devices. *ACS Nano* **8**, 316–322 (2014).
55. Chen, J.-Z., Ko, W.-Y., Yen, Y.-C., Chen, P.-H. & Lin, K.-J. Hydrothermally processed TiO₂ nanowire electrodes with antireflective and electrochromic properties. *ACS Nano* **6**, 6633–6639 (2012).
56. Shao, H. et al. Unraveling the charge storage mechanism of Ti₃C₂T_x MXene electrode in acidic electrolyte. *ACS Energy Lett.* **5**, 2873–2880 (2020).
57. Anayee, M. et al. Role of acid mixtures etching on the surface chemistry and sodium ion storage in Ti₃C₂T_x MXene. *Chem. Commun.* **56**, 6090–6093 (2020).
58. Neff, V. D. Electrochemical oxidation and reduction of thin films of Prussian blue. *J. Electrochem. Soc.* **125**, 886–887 (1978).

Acknowledgements

This work was supported by the Fluid Interface Reactions, Structures, and Transport (FIRST) Center, an Energy Frontier Research Center (EFRC) funded by the US Department of Energy, Office of Science and Office of Basic Energy Sciences. D.Z. and Y.G. also acknowledge funding for MXene synthesis from NSF Grant DMR-2041050.

Author contributions

D.Z., X.W. and Y.G. planned the research. D.Z. R.W. and X.W. designed the experiments. D.Z. synthesized and characterized all materials, performed in situ experiments and analysed data. R.W. developed in situ data analysis tools and protocols. D.Z. wrote the paper and R.W., X.W. and Y.G. edited and reviewed the paper.

Competing interests

The authors declare no competing interests.

Additional information

Supplementary information The online version contains supplementary material available at <https://doi.org/10.1038/s41560-023-01240-9>.

Correspondence and requests for materials should be addressed to Xuehang Wang or Yury Gogotsi.

Peer review information *Nature Energy* thanks Obaidallah Munteshari, Jean-Marie Tarascon and Wei Wang for their contribution to the peer review of this work.

Reprints and permissions information is available at www.nature.com/reprints.

Publisher's note Springer Nature remains neutral with regard to jurisdictional claims in published maps and institutional affiliations.

Springer Nature or its licensor (e.g. a society or other partner) holds exclusive rights to this article under a publishing agreement with the author(s) or other rightsholder(s); author self-archiving of the accepted manuscript version of this article is solely governed by the terms of such publishing agreement and applicable law.

© The Author(s), under exclusive licence to Springer Nature Limited 2023